Self-Supervised Learning for Image Super-Resolution and Deblurring

Jérémy Scanvic^{1,2} Mike Davies¹ Patrice Abry² Julián Tachella²

School of Engineering, University of Edinburgh Edinburgh, EH9 3FB, UK ² Laboratoire de Physique, CNRS, ENSL Lyon, F-69364, France

Abstract

Self-supervised methods have recently proved to be nearly as effective as supervised methods in various imaging inverse problems, paving the way for learning-based methods in scientific and medical imaging applications where ground truth data is hard or expensive to obtain. This is the case in magnetic resonance imaging and computed tomography. These methods critically rely on invariance to translations and/or rotations of the image distribution to learn from incomplete measurement data alone. However, existing approaches fail to obtain competitive performances in the problems of image super-resolution and deblurring, which play a key role in most imaging systems. In this work, we show that invariance to translations and rotations is insufficient to learn from measurements that only contain low-frequency information. Instead, we propose a new self-supervised approach that leverages the fact that many image distributions are approximately scale-invariant, and that can be applied to any inverse problem where highfrequency information is lost in the measurement process. We demonstrate throughout a series of experiments on real datasets that the proposed method outperforms other selfsupervised approaches, and obtains performances on par with fully supervised learning¹.

1. Introduction

Inverse problems are ubiquitous in scientific imaging and medical imaging. Linear inverse problems are generally modeled by the forward process

$$y = Ax + \varepsilon, \tag{1}$$

where $y \in \mathbb{R}^m$ represents the observed measurements, $x \in \mathcal{X} \subset \mathbb{R}^n$ represents the signal, $A \in \mathbb{R}^{m \times n}$ is the forward operator, and $\varepsilon \in \mathbb{R}^m$ depicts the noise corrupting the measurements. In this paper, we focus on additive

white Gaussian noise but our results can easily be generalized for other noise distributions, e.g. Poisson, or mixed Gaussian-Poisson. Recovering x from the noisy measurements is generally ill-posed. In many cases, the forward operator is rank-deficient, e.g. when the number of measurements is less than image pixels count, that is m < n. Moreover, even when the forward operator is not rank-deficient, it might still be ill-conditioned, and reconstructions might be very sensible to noise (e.g., in image deblurring problems).

There is a wide range of approaches for solving the inverse problem, i.e., recovering x from y. Classical methods rely on hand-crafted priors, e.g. a total variation, together with optimization algorithms to obtain a reconstruction that agrees with the observed measurements and the chosen prior [6]. These model-based approaches often obtain suboptimal results due to a mismatch between the true image distribution and the hand-crafted priors. An alternative approach leverages a dataset of reference images and associated measurements in order to train a reconstruction model. While this approach generally obtains state-of-theart performance, it is often hard to apply it in problems where ground truth images are expensive or even impossible to obtain.

In recent years, self-supervised methods have highlighted the possibility of learning from measurement data alone, thus bypassing the need for ground truth references. These methods focus either on taking care of noisy data or a rank-deficient operator. Noise can be handled through the use of Stein's unbiased risk estimator if the noise distribution is known [20], or via Noise2x techniques [2, 16, 17] which require milder assumptions on the noise distribution such as independence across pixels [2]. Rank-deficient operators can be handled using measurement data associated with multiple measurement operators A_1, \ldots, A_G (each with a different nullspace) [5, 31], or by assuming that the image distribution is invariant to certain groups of transformations such as translations or rotations [7, 8].

Self-supervised image deblurring methods have been proposed for deblurring with multiple (known) blur ker-

¹The code is available at https://github.com/jscanvic/Scale-Equivariant-Imaging

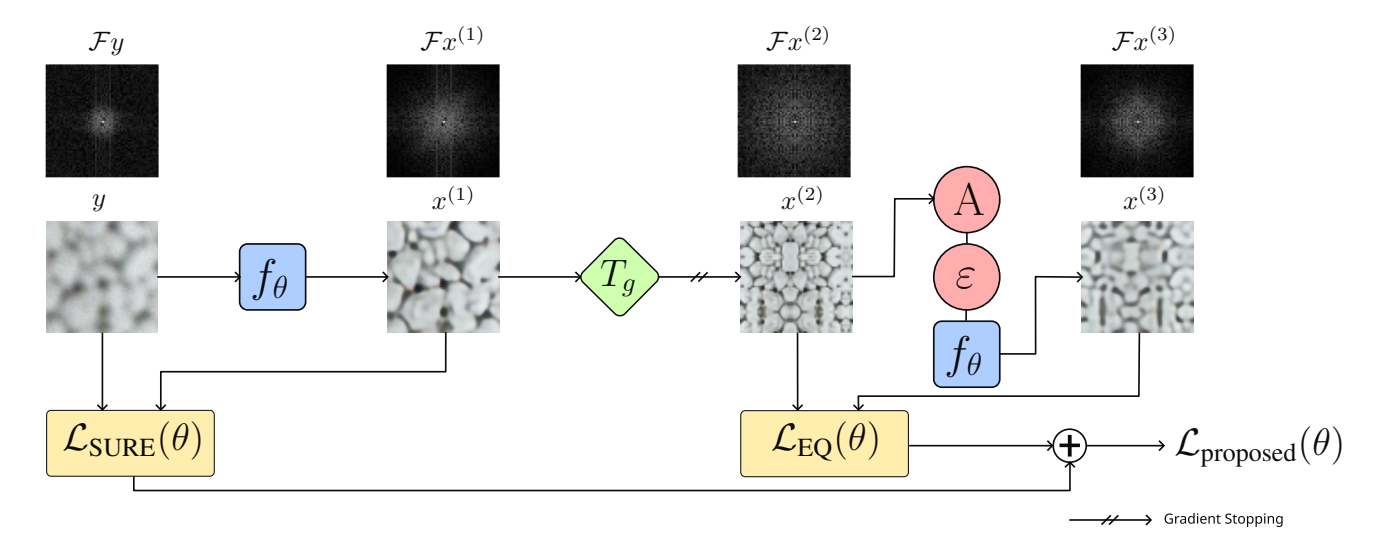


Figure 1. Solving image super-resolution and deblurring without ground truth images. Our method consists in training a deep neural network f_{θ} to learn the reconstruction function $f: y \mapsto x$ using noisy measurements $y = Ax + \varepsilon$ only, by minimizing a new self-supervised loss $\mathcal{L}_{\text{proposed}}(\theta)$ which leverages the scale-invariance property of common signal distributions. The loss is the sum of the SURE loss $\mathcal{L}_{\text{SURE}}(\theta)$ which penalizes reconstruction error in the measurement domain, and of the equivariant loss $\mathcal{L}_{\text{EQ}}(\theta)$ by viewing $x^{(1)} = f_{\theta}(y)$ as a ground truth which might lack high-frequency content, and the downscaled image $x^{(2)} = T_g x^{(1)}$ as another one which has high-frequency content, and finally by penalizing the mean squared error of the reconstruction $x^{(3)}$ obtained from a noisy measurement of $x^{(2)}$. The difference in high-frequency content is shown by $\mathcal{F}x^{(1)}$ and $\mathcal{F}x^{(2)}$, where \mathcal{F} is the discrete Fourier transform. One of our key contributions is stopping the gradient of $x^{(2)}$ during the stochastic gradient descent (see Section 4 for details).

nels [22], however this assumption is not verified in many applications. Moreover, self-supervised methods that rely on a single operator (e.g., a single blur kernel) [7, 8], have not been applied to inverse problems with a single forward operator that removes high-frequency information such as image super-resolution and image deblurring, except for methods exploiting internal/external patch recurrence [28] which assume noiseless measurements, thus not being easily generalizable to other inverse problems.

Image deblurring and super-resolution are two inverse problems particularly difficult to solve using self-supervised methods. The former is severely ill-conditioned, and the latter is rank-deficient. This makes methods that minimize the measurement consistency error inapplicable as they cannot retrieve any information that lies within the nullspace [7] or where the forward operator is ill-conditioned, whenever there is even the slightest amount of noise present.

In this work, we propose a new self-supervised loss for training reconstruction networks for super-resolution and image deblurring problems which relies on the assumption that the underlying image distribution is scale-invariant, and can be easily applied to any linear inverse problem, as long as the forward process is known. Figure 1 shows an overview of that loss. The main contributions are the following:

1. We propose a new self-supervised loss based on scaleinvariance for training reconstruction networks, which

- can be applied to any linear inverse problem where high-frequency information is lost by the forward operator.
- 2. Throughout a series of experiments, we show that the proposed method outperforms other self-supervised learning methods, and obtains a performance on par with fully supervised learning.

2. Related work

Supervised image reconstruction Most state-of-the-art super-resolution and image deblurring methods rely on a dataset containing ground truth references [9, 18, 26, 34]. However, in many scientific imaging problems such as fluorescence microscopy and astronomical imaging, having access to high-resolution images can be difficult, or even impossible [3].

Prior-based approaches A family of super-resolution and image deblurring methods rely on plug-and-play priors [14] and optimization methods. Other approaches rely on the inductive bias of certain convolutional architectures, i.e., the deep image prior [25, 32]. There are other methods that combine both techniques [19]. However, these approaches can provide sub-optimal results if the prior is insufficiently adapted to the problem.

SURE Stein's unbiased risk estimator is a popular strategy for learning from noisy measurement data alone, which requires knowledge of the noise distribution [10, 20, 29]. However, for image super-resolution and image deblurring, the forward operator is typically either rank-deficient or at least severely ill-conditioned, and the SURE estimates can only capture discrepancies in the range of the forward operator.

Noise2x methods The Noise2Noise method [17] shows that it is possible to learn a denoiser in a self-supervised fashion if two independent noisy realizations of the same image are available for training, without explicit knowledge of the noise distribution. Related methods extend this idea to denoising problems where a single noise realization is available, e.g. Noise2Void [16] and Noise2Self [2], and to general linear inverse problems, e.g., Noise2Inverse [13]. However, all of these methods crucially require that the forward operator is invertible and well-conditioned, which is not the case for super-resolution and most deblurring problems.

Equivariant imaging The equivariant imaging (EI) method leverages the invariance of typical signal distributions to rotations and/or translations to learn from measurement data alone, in problems where the forward operator is incomplete such as sparse-angle tomography, image inpainting and magnetic resonance imaging [7, 8, 11]. However, this approach requires the forward operator to not be equivariant to the rotations or translations. The superresolution problems and image deblurring problems with an isotropic blur kernel do not verify this condition, and EI methods cannot be used.

Patch recurrence methods Internal patch recurrence of natural images can be exploited to learn to super-resolve images without high-resolution references [28]. However, while this self-supervised learning method can be extended to collections of low-resolution images via external patch recurrence, it cannot be easily generalized to more general inverse problems (e.g., image deblurring) and noisy measurement data. The method proposed in this work generalizes the idea of patch recurrence to scale-invariance and can be applied to any imaging inverse problem where high-frequency information is missing.

3. Background

In this section, we review existing supervised and selfsupervised learning approaches for the problems of image super-resolution and image deblurring. We focus on reconstruction methods that train a reconstruction network $f_{\theta}: y \mapsto x$ which maps a low-resolution or blurry measurement y to a high-resolution image x.

Super-resolution and image deblurring The problem of image super-resolution consists in restoring a high-resolution image from a low-resolution one. It can be viewed as a linear inverse problem whose forward operator is defined by $Ax = (k*x)\downarrow_j$; where * is the convolution operator², $k \in \mathbb{R}^n$ is an antialiasing kernel, and \downarrow_j is the downsampling operator which keeps 1 every j pixels in the vertical and horizontal directions. The problem of image deblurring consists in restoring a sharp image from a blurry one. It can be viewed as a linear inverse problem whose forward operator is defined by Ax = k*x, where $k \in \mathbb{R}^n$ is a blur kernel. In both problems, we assume that the measurements are corrupted by i.i.d. Gaussian noise of standard deviation σ .

Supervised loss Supervised methods typically consist in minimizing a loss which is meant to enforce $f_{\theta}(y) = x$ for all $x \in \mathcal{X} \subset \mathbb{R}^n$, i.e.

$$\mathcal{L}_{SUP}(\theta) = \sum_{i=1}^{N} ||f_{\theta}(y_i) - x_i||_2^2.$$
 (2)

Although the supervised loss is expressed here in terms of the ℓ^2 -norm, other losses such as the ℓ^1 -norm are sometimes preferred [18]. While most methods adopt this approach (often including other perceptual losses [4]), they cannot be applied to the setting where high-resolution targets x_i are not available.

Self-supervision via patch recurrence Inspired by the zero-shot super-resolution [28] and Noisier2Noise [21] methods, it is possible to use the measurements y_i as ground truth targets, and compute corresponding corrupted inputs applying the forward operator to y, i.e.,

$$z = Ay + \tilde{\varepsilon} \tag{3}$$

where $\tilde{\varepsilon}$ is sampled from a zero-mean Gaussian distribution with the same standard deviation. Then, a self-supervised loss is constructed as

$$\mathcal{L}_{CSS}(\theta) = \sum_{i=1}^{N} ||y_i - f_{\theta}(z_i)||_2^2.$$
 (4)

which we name Classic Self-Supervised (CSS) loss. This approach is only valid when measurements y can be interpreted as images, such as in a super-resolution or image deblurring problems [28], however, it is unclear whether it

²Here for simplicity we consider circular convolution.

is effective for solving general problems, e.g. compressed sensing.

This method has been shown to be very effective in noiseless super-resolution problems [28] where the signal distribution is scale-invariant. However, this approach is not well-adapted to problems with noise or arbitrary blurring kernels, where the measurements are far from ground truth images, even if the signal distribution is approximately scale-invariant.

SURE loss The SURE loss [8, 20] is a self-supervised loss that serves as an unbiased estimator of the mean squared error (MSE) in measurement space

$$\mathbb{E}_{(x,y)} \| A f_{\theta}(y) - A x \|_{2}^{2}, \tag{5}$$

which does not require access to ground truth signals x. The SURE loss for measurements corrupted by Gaussian noise of standard deviation σ [8] is given by:

$$\mathcal{L}_{SURE}(\theta) = \sum_{i=1}^{N} \frac{1}{m} ||Af_{\theta}(y_i) - y_i||_2^2 + \sigma^2 - \frac{\sigma^2}{m} \sum_{i=1}^{m} \frac{\delta f_i}{\delta y_i}(y),$$

In practice, we approximate the divergence term using a Monte-Carlo estimate [24] (see the appendix for more details on the implementation).

It is worth noting that, in the noiseless setting, i.e. $\sigma = 0$, the SURE loss is equal to a measurement consistency constraint, $Af_{\theta}(y) = y$

$$\mathcal{L}_{MC}(\theta) = \sum_{i=1}^{N} \frac{1}{m} ||Af_{\theta}(y_i) - y_i||_2^2.$$
 (6)

This loss does not penalize the reconstructions in the nullspace of A. In the setting of super-resolution and image deblurring, the nullspace of the operator is associated with the high-frequencies of the image x, and thus training against the SURE loss alone fails to reconstruct the high-frequency content.

Equivariant imaging The equivariant imaging approach [7], offers a way to learn in the nullspace of the operator A, by leveraging some prior knowledge about the invariances of the signal distribution. If the support of the signal distribution, i.e. the signal set \mathcal{X} , is invariant to a group of transformations $\{T_g\}_{g=1}^G$, then we have that for any signal x, $x' = T_g x$ also is a valid signal, and thus a measurement y = Ax can also be interpreted as $y = A_g x'$ where $A_g = AT_g$ is a forward operator that might differ from A. This simple observation provides *implicit* access to a family of operators $\{AT_g\}_{g=1}^G$, which might have different nullspaces. A necessary condition for learning is that

the matrix

$$M = \sum_{g \in \mathcal{G}} T_g^{\top} A^{\top} A T_g \in \mathbb{R}^{n \times n} \tag{7}$$

has full rank, and in particular that A is not equivariant to the transformations [31]. Unfortunately, for imaging problems such as super-resolution and image deblurring, the forward operator A is equivariant to a group of rotations and/or translations T_g , which means the matrix in (7) is rank-deficient, and thus there is not enough information for learning in the nullspace of A. We formalize this observation with the following propositions:

Proposition 1. A blur operator with an isotropic kernel k is equivariant to translations and rotations.

Proposition 2. A downsampling operator with an ideal anti-aliasing filter k is equivariant to translations and rotations.

We provide the proofs for both propositions in the appendix. This result leads us to choose downscaling transformations, for which both forward operators are not equivariant. Downscale transformations constitute a semigroup (there are no inverse operations) acting on idealized bandlimited (digital) images [12, 33]. In particular, for such digital images, the associated upscaling transformations do not provide proper inverses. Fortunately, although the blur and downsampling operators are equivariant to shifts and rotations, both are not equivariant to downscalings:

Theorem 1. Consider the action by a semigroup of down-scaling transformations with circular padding $\{T_g\}$ with scales $g \in \{1/2, 1/3, \ldots\}$. If the forward operator A is a blur operator with an isotropic kernel or a downsampling operator with an ideal anti-aliasing filter, then it is not equivariant to downscalings.

The proof is included in the appendix.

4. Proposed method

In order to solve the problems of image super-resolution and image deblurring, we train a deep neural network as the reconstruction function $f_{\theta}: y \mapsto x$, with learnable weights $\theta \in \mathbb{R}^p$. We propose to minimize the training loss

$$\mathcal{L}_{\text{proposed}}(\theta) = \mathcal{L}_{\text{SURE}}(\theta) + \alpha \mathcal{L}_{\text{EO}}(\theta), \tag{8}$$

where $\alpha > 0$ is a trade-off parameter, $\mathcal{L}_{SURE}(\theta)$ is the SURE loss (3), and $\mathcal{L}_{EQ}(\theta)$ is the equivariant loss introduced below, which is similar to the robust equivariant imaging loss [8]. In all experiments, we set $\alpha = 1$. The two contributions of our method are the use of the action by downscaling transforms instead of the action by shifts or by rotations,

and stopping the gradient during the forward pass (details are explained below).

In the forward pass, we first compute $x_{i,\theta}^{(1)} = f_{\theta}(y_i)$, which we view as an estimation of the ground truth signal x. Next, we compute $x_i^{(2)} = T_g x_{i,\theta}^{(1)}$, where T_g is a downscale transformation of scale g, without propagating the gradient, which effectively leaves $\nabla_{\theta} x_i^{(2)} = 0$. Finally, we compute $x_{i,\theta}^{(3)} = f_{\theta}(Ax_i^{(2)} + \tilde{\varepsilon})$ where $\tilde{\varepsilon}$ is sampled from $\mathcal{N}(0, \sigma^2 I)$. The three terms are used to compute $\mathcal{L}_{\text{SURE}}$ and \mathcal{L}_{EO} (see Figure 1), where \mathcal{L}_{EO} is defined as

$$\mathcal{L}_{EQ}(\theta) = \sum_{i=1}^{N} \frac{1}{n} \|x_{i,\theta}^{(3)} - x_i^{(2)}\|_2^2.$$
 (9)

Downscale transformations In all experiments, T_g is implemented using the scale function from the kornia library [27], with nearest interpolation, reflection padding, aligned corners, and a different random transform-origin for each call and each element in a batch. The scale factor is uniformly sampled from $\{.5, .75\}$. Figure 2 shows an example of transformations.

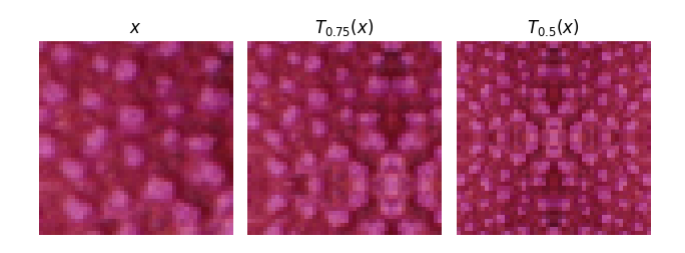


Figure 2. Implementation of scale transforms T_g . The transform center is set to the top-left corner, (left) is a ground-truth patch x, (middle) is the transformed patch $T_{.75}(x)$ for a .75 scale factor, and (right) is the transformed patch $T_{.5}(x)$ for a .5 scale factor.

Transform	Stop	Div2K-Train		Div2K-Val	
		PSNR	SSIM	PSNR	SSIM
Scale	√	25.9	0.760	26.3	0.784
Shift	\checkmark	25.1	0.714	25.3	0.743
Shift	×	23.7	0.678	24.3	0.709
Rotation	\checkmark	25.3	0.724	25.7	0.753
Rotation	×	24.2	0.660	24.7	0.691

Table 1. **Comparison with equivariant imaging using shifts and rotations.** Stop is checked to denote stopping the gradient.

Gradient stopping The gradient-stopping step, which removes the dependence of $x_i^{(2)}$ on the network weights θ plays an important role in the self-supervised loss. Table 2 shows that gradient stopping boosts the performance

of the self-supervised network in a $2\times$ super-resolution problem by a significant amount, i.e. 3dB. In the appendix, we demonstrate empirically that the gradient stopping technique modifies the minima of the structure compared to the standard EI technique (no stopping).

Stop	Div2K-Train		Div2K-Val		
	PSNR	SSIM	PSNR	SSIM	
\checkmark	33.1	0.928	35.7	0.941	
×	30.3	0.874	32.6	0.893	

Table 2. **Effect of gradient stopping.** When stop is checked, the gradient is stopped, otherwise it is not.

Comparison to self-supervision via patch recurrence Both the proposed loss and the CSS loss in (4) leverage scale-invariance to form a self-supervised loss. The CSS method requires that A is a downsampling transformation and that the noise ε is sufficiently small, such that $Ay \approx x'$ for some x' which also belongs to the dataset. The proposed method exploits scale-invariance on the reconstructed images, thus being applicable to any operator A. Thus, for the super-resolution problems with a small amount of noise, we expect to obtain a similar performance with both methods, whereas in the more challening image deblurring problem we expect to observe a different performance across methods.

5. Experiments

Dataset Throughout the experiments, we use datasets containing pairs of ground truth images and noisy measurements. The ground truth images are obtained from Div2K [1], a dataset containing high-resolution images (around 1500×1500 pixels) depicting natural scenes (e.g. buildings, landscapes, animals), which we resize to a resolution around 300×300 pixels for image deblurring, in order to get significant degradation with reasonably small kernels. For image super-resolution, the clean measurements are computed from the ground truth images using the MAT-LAB function imresize, with a downsampling factor of 2 or 4, bicubic interpolation and an antialiasing filter, and for image deblurring, using circular convolution with a Gaussian kernel or a box kernel. We denote the blur level by $R_{\rm blur}$, i.e. the standard deviation for Gaussian kernels, and the radius for Box kernels. The noisy measurements are obtained by further degrading clean measurements using additive white Gaussian noise with standard deviation σ . Each dataset contains 810 pairs, 800 of which are used to train models, and 10 which are used for validation only. Instead of training on full images, we randomly crop training patch pairs at every epoch such that input patches have size 48×48 .

Network architecture To ensure a fair comparison, all the models in the experiments are built upon the SwinIR architecture [18], which is a state-of-the-art architecture for image reconstruction. It is made of convolutional layers, but it is not fully convolutional since it also contains multi-head self-attention layers followed by a multi-layered perceptron layer. It also contains an optional upsampling layer which we use for super-resolution but not for image deblurring.

Performance metrics We measure the reconstruction performance using the PSNR and SSIM metrics on the luminance channel (Y) in the YCbCr color space, as is often done in the image reconstruction literature [18]. We compute the reconstruction performance on 10 training pairs, and on the 10 validation pairs. It is important to note that computing reconstruction performance on training pairs is relevant for self-supervised methods since they do not learn from ground truth images during training.

	σ	Div2K-Train		Div2K-Val	
		PSNR	SSIM	PSNR	SSIM
sup	0	33.3	0.929	35.9	0.941
css		33.2	0.929	35.9	0.942
proposed		33.1	0.928	35.7	0.941
$y \uparrow_2$		30.2	0.883	32.4	0.900
sup	25/255	28.6	0.778	29.9	0.799
css		28.0	0.764	29.0	0.778
proposed		28.1	0.786	29.1	0.802
$y \uparrow_2$		24.0	0.483	24.3	0.477

Table 3. Reconstruction performance of the evaluated methods on the $\times 2$ image super-resolution problem. The bicubic upsampling of the noisy measurement $y = Ax + \varepsilon$ is denoted as $y \uparrow_2$.

	σ	Div2K-Train		Div2K-Val		
		PSNR	SSIM	PSNR	SSIM	
sup	10/255	26.8	0.743	28.0	0.760	
css		26.6	0.736	27.8	0.755	
proposed		26.5	0.718	27.6	0.733	
$y \uparrow_4$		25.1	0.647	26.3	0.670	
sup	25/255	25.3	0.686	26.3	0.701	
css		25.2	0.679	26.1	0.695	
proposed		25.0	0.656	25.9	0.674	
$y \uparrow_4$		22.5	0.449	23.0	0.459	

Table 4. Reconstruction performance of the evaluated methods on the $\times 4$ image super-resolution problem. The bicubic upsampling of the noisy measurement $y=Ax+\varepsilon$ is denoted as $y{\uparrow}_4$.

	σ	$R_{ m blur}$	Div2K-Train		Div2K-Val	
			PSNR	SSIM	PSNR	SSIM
sup	$\frac{5}{255}$	1.0	30.8	0.917	31.0	0.916
proposed			30.2	0.896	30.5	0.899
css			29.1	0.886	29.7	0.895
\overline{y}			26.7	0.787	27.2	0.808
Ax			27.1	0.832	27.7	0.852
sup		2.0	26.1	0.773	26.4	0.795
proposed			25.9	0.760	26.3	0.784
css			24.6	0.696	25.1	0.726
y			23.1	0.594	23.6	0.626
Ax			23.4	0.636	23.8	0.666
sup		3.0	24.1	0.681	24.3	0.702
proposed			24.0	0.653	24.2	0.673
css			23.3	0.614	23.7	0.646
\overline{y}			21.7	0.493	21.9	0.523
Ax			21.8	0.531	22.0	0.561

Table 5. Reconstruction performance of the evaluated methods on the Gaussian deblurring problem. The noisy measurements are denoted by $y=Ax+\varepsilon$, and clean measurements by Ax.

σ	$R_{ m blur}$	Div2K-Train		Div2K-Val	
		PSNR	SSIM	PSNR	SSIM
5 255	2	28.9	0.864	29.1	0.859
200		27.8	0.837	27.9	0.834
		26.4	0.796	26.7	0.806
		23.8	0.620	24.3	0.661
		24.0	0.661	24.5	0.701
	3	27.3	0.809	27.5	0.807
		26.0	0.766	26.3	0.773
		24.6	0.703	25.0	0.726
		22.4	0.529	22.8	0.565
		22.6	0.568	22.9	0.603
	4	25.7	0.743	25.8	0.744
		24.8	0.707	25.1	0.712
		23.5	0.627	23.8	0.657
		21.5	0.469	21.8	0.501
		21.6	0.506	21.9	0.538
	5/255	$\frac{5}{255}$ 2	$\begin{array}{c cccc} & & PSNR \\ \hline \frac{5}{255} & 2 & 28.9 \\ 27.8 \\ 26.4 \\ & & & & \\ 23.8 \\ \hline & & & & \\ 24.0 \\ & & & & \\ & & & \\ & & & & \\ & & & \\ & & & & \\ & & \\ & & & \\ & & & \\ & & & \\ & & & \\ & & \\ & & & \\ & & \\ & & & \\ & & $	$\begin{array}{c ccccccccccccccccccccccccccccccccccc$	$\begin{array}{c ccccccccccccccccccccccccccccccccccc$

Table 6. Reconstruction performance of the evaluated methods on the box deblurring problem. The noisy measurements are denoted by $y = Ax + \varepsilon$, and clean measurements by Ax.

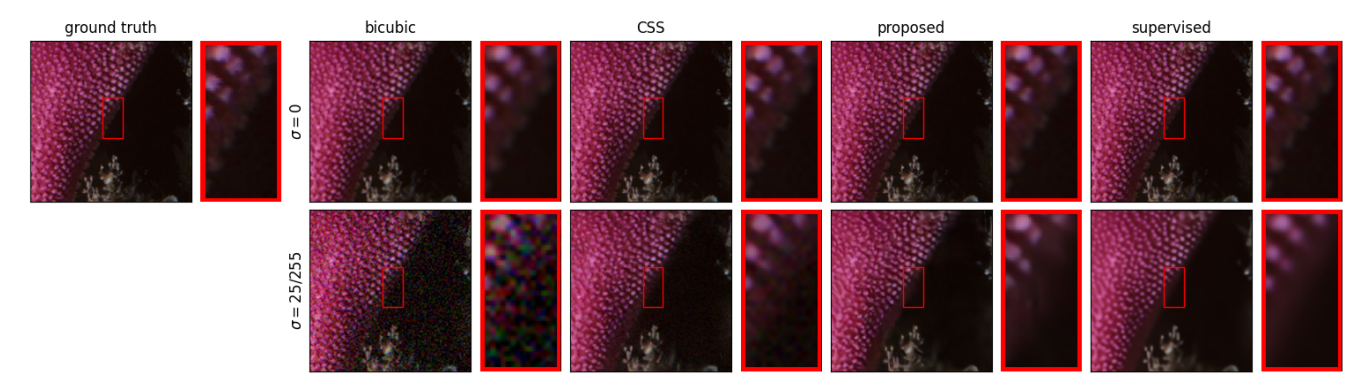


Figure 3. Sample reconstructions for the evaluated methods on the $\times 2$ image super-resolution problem. The sample is taken from the training split.

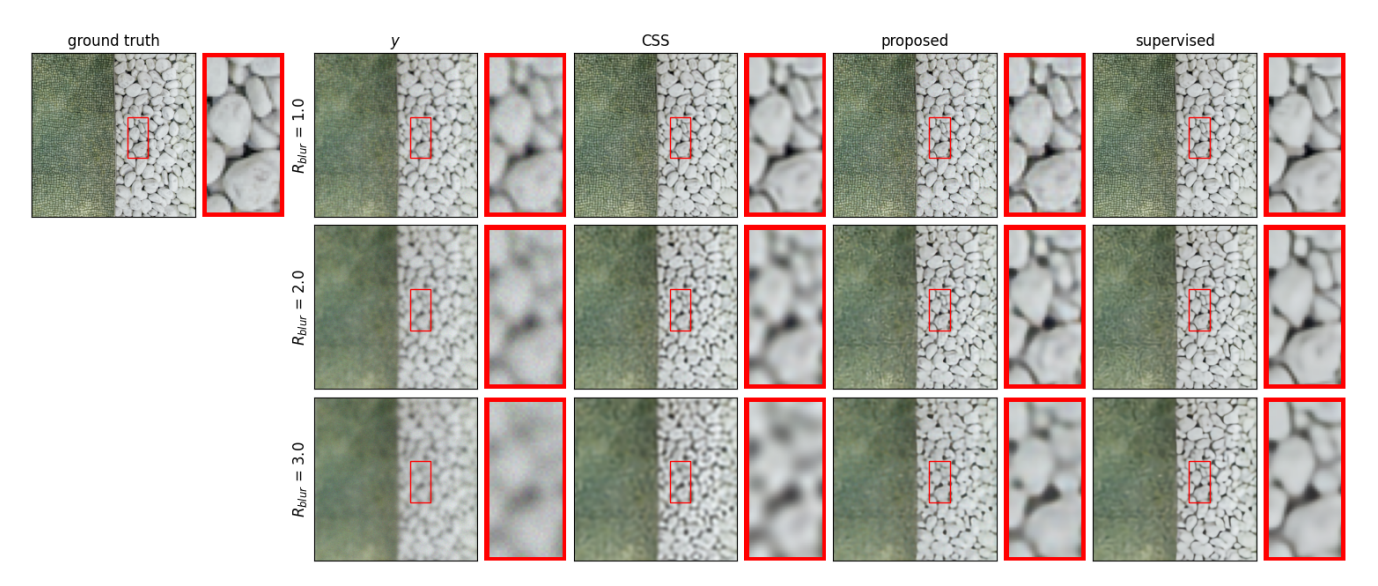


Figure 4. Sample reconstructions for the evaluated methods on the Gaussian deblurring problem. The sample is taken from the training split.

Training details We train models for 500 epochs against training losses \mathcal{L}_{SUP} , \mathcal{L}_{CSS} and $\mathcal{L}_{\text{proposed}}$. We use an initial learning rate of $2 \cdot 10^{-4}$ for super-resolution, and of $5 \cdot 10^{-4}$ for deblurring. We use a multi-step scheduler that divides the learning rate by a factor of 2 at epochs 250, 400, 450, and 475. We use a batch size of 16 for super-resolution, and of 8 for deblurring. We use the Adam optimizer [15] with $\beta = (.9, .99)$ and no weight decay. The experiments are performed using 4 GPUs on a SIDUS solution [23].

Super-resolution experiments For $\times 2$ image superresolution, Figure 3 shows no significant visual difference between images obtained using the supervised, proposed, and CSS methods in the noiseless case. For noise level $\sigma=25/255$, we observe that some noise is present in the dark region on the image obtained using the CSS method, but not on those obtained using supervised and proposed methods. We also observe that the image obtained using

the supervised method is slightly smoother than the ground truth image, and images obtained using the proposed and CSS methods when looking at the light pimples.

Table 3 shows that the proposed method performs almost as well as the supervised method (-0.4 dB loss on average), and similarly as the CSS method, as predicted (+0.0 dB gain on average). Table 4 shows similar results for $\times 4$ image super-resolution.

Gaussian deblurring experiments Figure 4 shows that the CSS method produces blurrier images than the supervised and proposed methods, for all three blur levels, and especially so for the two highest blur levels. For the highest blur level, we observe that the contour between two rocks on the upper right part of the zoomed-in region is visible on images obtained using the proposed and CSS methods, but is not visible on the image obtained using the supervised method.

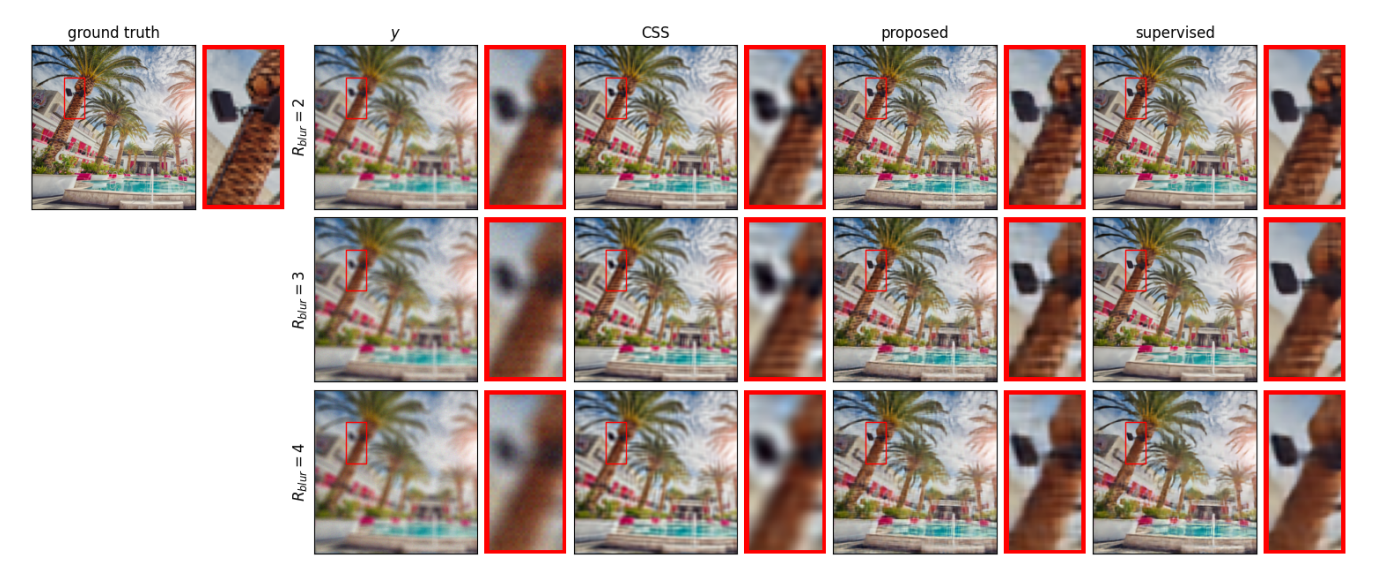


Figure 5. Sample reconstructions for the evaluated methods on the box deblurring problem. The sample is taken from the training split.

Table 5 shows that the proposed method performs significantly better than the CSS method (+1.0 dB gain on average) and almost as good as the supervised method (-0.3 dB loss on average).

Table 1 shows that for $R_{\rm blur}=2.0$, the proposed method (using downscaling transformations) performs better than equivariant imaging methods using shifts or rotations, even when stopping the gradient. Moreover, it shows that stopping the gradient improves the performance of the latter methods by approximately 1 dB gain.

Box deblurring experiments Figure 5 shows that images obtained using the CSS method are blurrier than images obtained using the supervised and proposed methods, for all three blur levels. We observe horizontal and vertical artifacts on the image obtained using the supervised method for medium blur level, on those obtained using the proposed method for medium and high levels, and on those obtained using the CSS method for all three levels, but not on other images.

Table 6 shows that the proposed method performs better than the CSS method ($+1.3~\mathrm{dB}$ gain on average) and $-1.1~\mathrm{dB}$ worse than the supervised method. Overall, we observe that the proposed method performs almost as well as the supervised method, and better than the CSS method.

6. Conclusion

In this work, we propose a new self-supervised method for solving the problems of image super-resolution and image deblurring which leverages the scale-invariance of typical image distributions. The experiments show that our method can be as effective as supervised methods while outperforming other self-supervised methods.

The proposed method extends the equivariant imaging loss to problems where high-frequency information is lost, which play a fundamental role in most imaging systems. The proposed method offers significant flexibility: i) the self-supervised loss can be used to train any network architecture, ii) the loss can be applied to any inverse problem, e.g. performing super-resolution in MRI, as long as the forward process is known, and iii) only a single forward operator is required.

While a theoretical analysis of necessary and sufficient conditions for learning from measurement data alone is available for the case where the transformations T_g are associated with a compact group, such as rotations and/or translations [30], the results do not hold for the action by scalings which form a semi-group [33] (as it does not have an inverse). The interesting question of what theoretical analysis model identification is possible in this scenario is left for future work.

References

- [1] Eirikur Agustsson and Radu Timofte. NTIRE 2017 Challenge on Single Image Super-Resolution: Dataset and Study. In 2017 IEEE Conference on Computer Vision and Pattern Recognition Workshops (CVPRW), pages 1122–1131, Honolulu, HI, USA, 2017. IEEE. 5
- [2] Joshua Batson and Loic Royer. Noise2Self: Blind Denoising by Self-Supervision. In *Proceedings of the 36th International Conference on Machine Learning*, pages 524–533. PMLR, 2019. ISSN: 2640-3498. 1, 3
- [3] Chinmay Belthangady and Loic A Royer. Applications, promises, and pitfalls of deep learning for fluorescence im-

- age reconstruction. *Nature methods*, 16(12):1215–1225, 2019. 2
- [4] Yochai Blau and Tomer Michaeli. The perception-distortion tradeoff. In *Proceedings of the IEEE conference on computer vision and pattern recognition*, pages 6228–6237, 2018. 3
- [5] Ashish Bora, Eric Price, and Alexandros G Dimakis. Ambientgan: Generative models from lossy measurements. In *International conference on learning representations*, 2018.
- [6] Antonin Chambolle and Thomas Pock. An introduction to continuous optimization for imaging. *Acta Numerica*, 25: 161–319, 2016.
- [7] Dongdong Chen, Julian Tachella, and Mike E. Davies. Equivariant Imaging: Learning Beyond the Range Space. In 2021 IEEE/CVF International Conference on Computer Vision (ICCV), pages 4359–4368, Montreal, QC, Canada, 2021. IEEE. 1, 2, 3, 4
- [8] Dongdong Chen, Julian Tachella, and Mike E. Davies. Robust Equivariant Imaging: a fully unsupervised framework for learning to image from noisy and partial measurements. In 2022 IEEE/CVF Conference on Computer Vision and Pattern Recognition (CVPR), pages 5637–5646, New Orleans, LA, USA, 2022. IEEE. 1, 2, 3, 4
- [9] Jiangxin Dong, Stefan Roth, and Bernt Schiele. Deep Wiener Deconvolution: Wiener Meets Deep Learning for Image Deblurring. In Advances in Neural Information Processing Systems, pages 1048–1059. Curran Associates, Inc., 2020. 2
- [10] Yonina C. Eldar. Generalized SURE for Exponential Families: Applications to Regularization. *IEEE Transactions on Signal Processing*, 57(2):471–481, 2009. Conference Name: IEEE Transactions on Signal Processing. 3
- [11] Ketan Fatania, Kwai Y. Chau, Carolin M. Pirkl, Marion I. Menzel, and Mohammad Golbabaee. Nonlinear Equivariant Imaging: Learning Multi-Parametric Tissue Mapping without Ground Truth for Compressive Quantitative MRI. In 2023 IEEE 20th International Symposium on Biomedical Imaging (ISBI), pages 1–4, 2023. ISSN: 1945-8452. 3
- [12] Luc MJ Florack, Bart M ter Haar Romeny, Jan J Koenderink, and Max A Viergever. Scale and the differential structure of images. *Image and vision computing*, 10(6):376–388, 1992.
- [13] Allard A. Hendriksen, Daniel M. Pelt, and K. Joost Batenburg. Noise2Inverse: Self-supervised deep convolutional denoising for tomography. *IEEE Transactions on Computational Imaging*, 6:1320–1335, 2020. arXiv:2001.11801 [cs, eess, stat]. 3
- [14] Ulugbek S Kamilov, Charles A Bouman, Gregery T Buzzard, and Brendt Wohlberg. Plug-and-play methods for integrating physical and learned models in computational imaging: Theory, algorithms, and applications. *IEEE Signal Process*ing Magazine, 40(1):85–97, 2023. 2
- [15] Diederik P Kingma and Jimmy Ba. Adam: A method for stochastic optimization. arXiv preprint arXiv:1412.6980, 2014. 7
- [16] Alexander Krull, Tim-Oliver Buchholz, and Florian Jug. Noise2Void Learning Denoising From Single Noisy Images. pages 2129–2137, 2019. 1, 3

- [17] Jaakko Lehtinen, Jacob Munkberg, Jon Hasselgren, Samuli Laine, Tero Karras, Miika Aittala, and Timo Aila. Noise2Noise: Learning Image Restoration without Clean Data. In *Proceedings of the 35th International Conference on Machine Learning*, pages 2965–2974. PMLR, 2018. ISSN: 2640-3498. 1, 3
- [18] Jingyun Liang, Jiezhang Cao, Guolei Sun, Kai Zhang, Luc Van Gool, and Radu Timofte. SwinIR: Image Restoration Using Swin Transformer. In 2021 IEEE/CVF International Conference on Computer Vision Workshops (ICCVW), pages 1833–1844, Montreal, BC, Canada, 2021. IEEE. 2, 3, 6
- [19] Gary Mataev, Peyman Milanfar, and Michael Elad. DeepRED: Deep Image Prior Powered by RED. pages 0– 0, 2019.
- [20] Christopher A. Metzler, Ali Mousavi, Reinhard Heckel, and Richard G. Baraniuk. Unsupervised Learning with Stein's Unbiased Risk Estimator, 2020. arXiv:1805.10531 [cs, stat]. 1, 3, 4
- [21] Nick Moran, Dan Schmidt, Yu Zhong, and Patrick Coady. Noisier2noise: Learning to denoise from unpaired noisy data. In *Proceedings of the IEEE/CVF Conference on Computer Vision and Pattern Recognition*, pages 12064–12072, 2020. 3
- [22] Yuhui Quan, Zhuojie Chen, Huan Zheng, and Hui Ji. Learning Deep Non-blind Image Deconvolution Without Ground Truths. In *Computer Vision ECCV 2022*, pages 642–659, Cham, 2022. Springer Nature Switzerland. 2
- [23] Emmanuel Quemener and Marianne Corvellec. Sidus—the solution for extreme deduplication of an operating system. *Linux Journal*, 2013(235):3, 2013. 7
- [24] Sathish Ramani, Thierry Blu, and Michael Unser. Montecarlo sure: A black-box optimization of regularization parameters for general denoising algorithms. *IEEE Transac*tions on image processing, 17(9):1540–1554, 2008. 4
- [25] Dongwei Ren, Kai Zhang, Qilong Wang, Qinghua Hu, and Wangmeng Zuo. Neural blind deconvolution using deep priors. In Proceedings of the IEEE/CVF Conference on Computer Vision and Pattern Recognition, pages 3341–3350, 2020. 2
- [26] Wenqi Ren, Jiawei Zhang, Lin Ma, Jinshan Pan, Xiaochun Cao, Wangmeng Zuo, Wei Liu, and Ming-Hsuan Yang. Deep Non-Blind Deconvolution via Generalized Low-Rank Approximation. In Advances in Neural Information Processing Systems. Curran Associates, Inc., 2018. 2
- [27] Edgar Riba, Dmytro Mishkin, Daniel Ponsa, Ethan Rublee, and Gary Bradski. Kornia: an Open Source Differentiable Computer Vision Library for PyTorch. In 2020 IEEE Winter Conference on Applications of Computer Vision (WACV), pages 3663–3672, Snowmass Village, CO, USA, 2020. IEEE. 5
- [28] Assaf Shocher, Nadav Cohen, and Michal Irani. Zero-Shot Super-Resolution Using Deep Internal Learning. In 2018 IEEE/CVF Conference on Computer Vision and Pattern Recognition, pages 3118–3126, Salt Lake City, UT, 2018, IEEE, 2, 3, 4
- [29] Charles M. Stein. Estimation of the Mean of a Multivariate Normal Distribution. The Annals of Statistics, 9(6):1135—

- 1151, 1981. Publisher: Institute of Mathematical Statistics.
- [30] Julian Tachella and Marcelo Pereyra. Equivariant Bootstrapping for Uncertainty Quantification in Imaging Inverse Problems, 2023. arXiv:2310.11838 [cs, eess, stat]. 8
- [31] Julián Tachella, Dongdong Chen, and Mike Davies. Sensing Theorems for Unsupervised Learning in Linear Inverse Problems. *Journal of Machine Learning Research*, 24(39): 1–45, 2023. 1, 4
- [32] Dmitry Ulyanov, Andrea Vedaldi, and Victor Lempitsky. Deep Image Prior. pages 9446–9454, 2018. 2
- [33] Daniel Worrall and Max Welling. Deep scale-spaces: Equivariance over scale. *Advances in Neural Information Processing Systems*, 32, 2019. 4, 8
- [34] Li Xu, Jimmy SJ Ren, Ce Liu, and Jiaya Jia. Deep Convolutional Neural Network for Image Deconvolution. In Advances in Neural Information Processing Systems. Curran Associates, Inc., 2014. 2

A. Additional experiments

Table 7 shows that the proposed method has better performance than equivariant imaging for ×2 super-resolution with noise level $\sigma = 25/255$.

Transform	Stop	Div2K-Train		Div2K-Val	
		PSNR	SSIM	PSNR	SSIM
Scale	✓	28.1	0.778	29.9	0.799
Shift	\checkmark	27.7	0.750	28.6	0.764
Shift	×	27.6	0.757	28.8	0.778
Rotation	\checkmark	27.9	0.780	29.0	0.797
Rotation	×	27.3	0.737	28.5	0.760

Table 7. Comparison with equivariant imaging using shifts and rotations for $\times 2$ super-resolution. Stop is checked to denote stopping the gradient.

B. Additional results

Figure 6 shows sample reconstructions for $\times 2$ super resolution with different noise levels σ . Figure 7 shows sample reconstructions for Gaussian deblurring with fixed noise standard deviation $\sigma = 5/255$ and different blur levels $R_{\rm blur}$. Figure 8 shows sample reconstructions for box deblurring with fixed noise standard deviation $\sigma = 5/255$ and different blur levels $R_{\rm blur}$.

C. Proofs of Proposition 1 and 2

In this section, we provide proofs for Proposition 1 and 2. For the sake of simplicity, we consider images $x \in \mathbb{R}^n$ with height and width equal to $n' = \sqrt{n}$, although the results can be generalized for any aspect ratio. Furthermore, we write $x_{l,s} \in \mathbb{R}$ to denote the pixel in the (l,s)th coordinate of x, where $l = 0, 1, \dots, n' - 1$ and $s = 0, 1, \dots, n' - 1$.

Discrete Fourier transform We use the spectral properties of downsampling with an ideal low-pass filter, expressed in terms of the 2D discrete Fourier transform $\mathcal{F} \in$ $\mathbb{C}^{n\times n}$ defined by

$$(\mathcal{F}x)_{l,s} = \sum_{p=0}^{n'-1} \sum_{q=0}^{n'-1} x_{p,q} e^{-2i\pi(lp+sq)/n'}$$
 (10)

where l, s = 0, ..., n' - 1.

2D circular convolutions In order to define blur and downsampling operators, we use the 2D circular convolution of a signal $x \in \mathbb{R}^n$ by a kernel $k \in \mathbb{R}^n$, defined by

$$(k*x)_{l,s} = \sum_{p=0}^{n'-1} \sum_{q=0}^{n'-1} k_{p,q} x_{(l-p)_{n'},(s-q)_{n'}},$$
(11)

where $l, s = 0, \ldots, n' - 1$, and $(l - p)_{n'}$ denotes the remainder of l-p divided by n'.

Blur and downsampling operators In this section, we consider a blur operator $B \in \mathbb{R}^{n \times n}$, defined as the 2D circular convolution by kernel $k \in \mathbb{R}^n$,

$$Bx = k * x, \ x \in \mathbb{R}^n, \tag{12}$$

and a downsampling operator $S \in \mathbb{R}^{m \times n}$, defined by

$$(Sx)_{l,s} = (k*x)_{rl,rs}, x \in \mathbb{R}^n,$$

where r = n'/m' is the downsampling factor, $m' = \sqrt{m}$, $k \in \mathbb{R}^n$ is an antialiasing kernel and $l, s = 0, \dots, m' - 1$. Without loss of generality, we focus on downsampling by a factor of 2, i.e. m' = n'/2 and r = 2, however, our results can easily be generalized for other integer factors.

Actions by shifts and rotations The action by shifts $T_{g_1,g_2}\in\mathbb{R}^{n\times n}$, with horizontal and vertical displacements $g_1,g_2=0,\ldots,n'-1$, is defined by

$$(T_{g_1,g_2}x)_{l,s} = x_{(l+g_1)_{n'},(l+g_2)_{n'}}, x \in \mathbb{R}^n,$$
 (13)

where $l, s = 0, \dots, n' - 1$, or equivalently in the Fourier basis

$$(\hat{T}_{q_1,q_2}\hat{x})_{l,s} = e^{2i\pi(lg_1 + sg_2)/n'}\hat{x}_{l,s},\tag{14}$$

where $\hat{T}_{g_1,g_2} = \mathcal{F}T_{g_1,g_2}\mathcal{F}^{-1} \in \mathbb{R}^{n \times n}$. The action by rotations $R_g \in \mathbb{R}^{n \times n}$, with angles of g = 10, 90, 180, 270 degrees, is defined by

$$(R_g x)_{l,s} = \begin{cases} x_{(l)_{n'},(s)_{n'}} & \text{if } g = 0, \\ x_{(-s)_{n'},(l)_{n'}} & \text{if } g = 90, \\ x_{(-l)_{n'},(-s)_{n'}} & \text{if } g = 180, \\ x_{(s)_{n'},(-l)_{n'}} & \text{if } g = 270, \end{cases}$$
(15)

where l, s = 0, ..., n' - 1.

Equivariance to shifts and rotations In this section, we prove that under mild conditions the blur operator B and the downsampling operator S are equivariant to actions by shifts T_g , and by rotations R_g . Because equivariance is a property relating an operator and a group acting on both its input and output spaces, we need to specify what group action on the output space we consider in each case. For the blur operator B, input and output spaces are equal, and we consider the action on its output space to be equal to the action on its input space.

For operator S and action by rotations R_a , we consider the action on the output space to be the action by rotations $\tilde{R}_g \in \mathbb{R}^{m \times m}, g = 0, 90, 180, 270,$ and for the action by shifts T_q , we consider the action on the output space to be

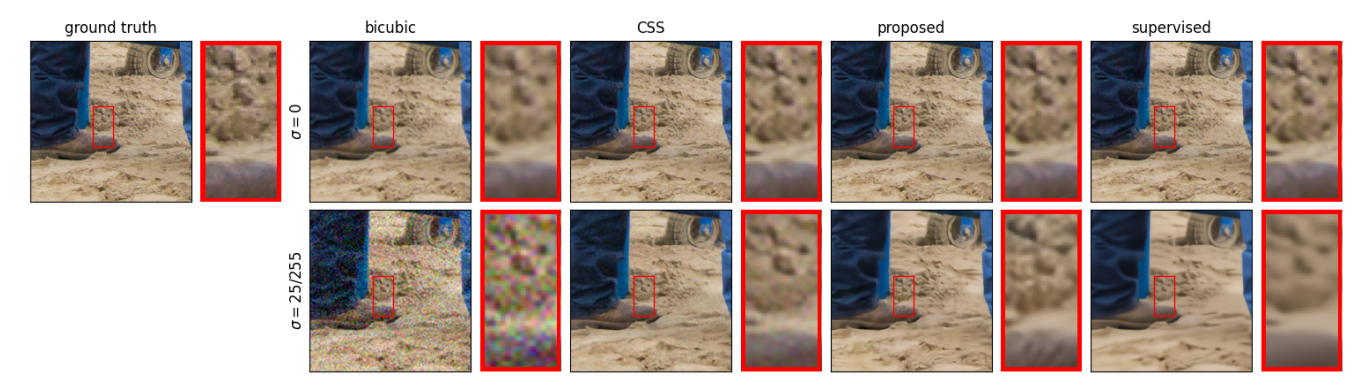


Figure 6. Sample reconstructions for the evaluated methods on the $\times 2$ image super-resolution problem. The sample is taken from the validation split.

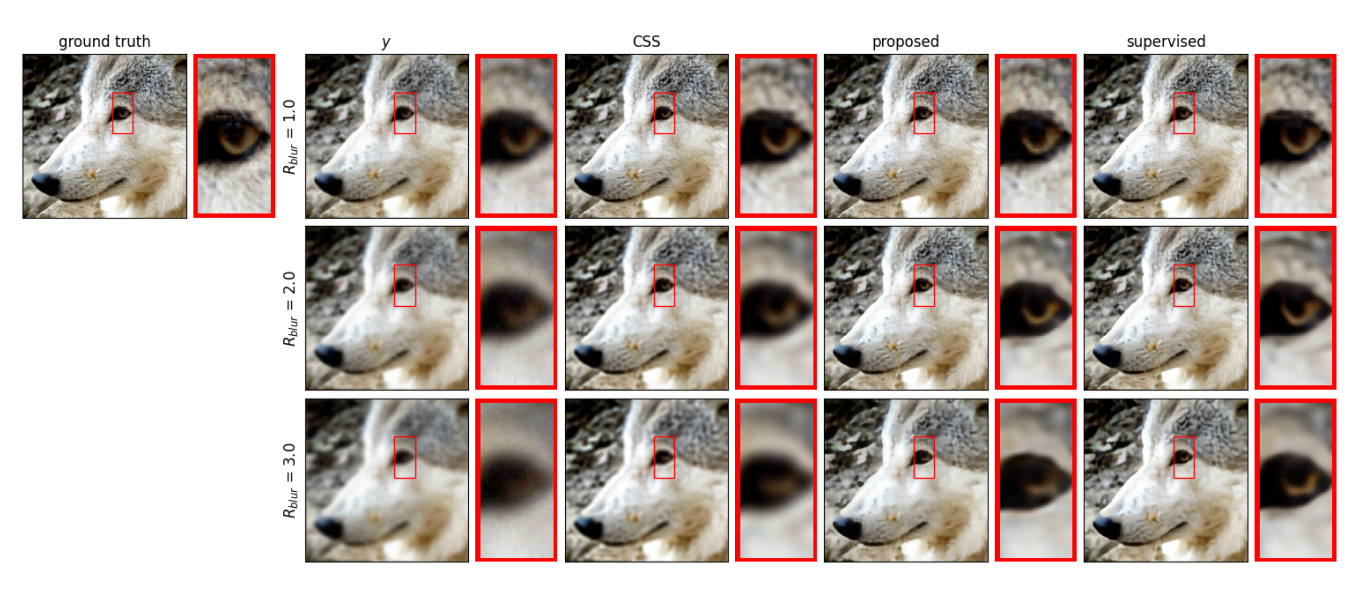


Figure 7. Sample reconstructions for Gaussian deblurring on the validation split, for methods sup, proposed, and css, and different blur standard deviations R_{blur} .

the translation by a displacement of g/2, defined in Fourier basis by

$$(\hat{\tilde{T}}_{q_1,q_2}\hat{x})_{l,s} = e^{2i\pi(lg_1/2 + sg_2/2)/m'}\hat{x}_{l,s}.$$
 (16)

In summary, we will prove that

$$BR_q = R_q B \text{ for } g = 0, 90, 180, 270$$
 (17)

$$SR_q = \tilde{R}_q S \text{ for } g = 0, 90, 180, 270$$
 (18)

$$BT_{g_1,g_2} = T_{g_1,g_2}B$$
 for $g_1,g_2 = 0,\dots,n'-1$ (19)

$$ST_{g_1,g_2} = \tilde{T}_{g_1,g_2}S$$
 for $g_1, g_2 = 0, \dots, n' - 1$. (20)

Isotropic kernels An isotropic kernel $k \in \mathbb{R}^n$ is a kernel that is invariant to rotations, in our case it satisfies

$$R_q k = k, \ g = 0, 90, 180, 270.$$
 (21)

Ideal anti-aliasing filter A downsampling operator S by factor 2 with ideal anti-aliasing filter $k \in \mathbb{R}^n$ satisfies

$$(\hat{S}\hat{x})_{(l)_{m'},(s)_{m'}} = (\hat{x})_{(l)_{n'},(s)_{n'}},\tag{22}$$

where $l, s = -(m'-1)/2, \ldots, (m'-1)/2$, assuming n' is even and m' is odd.

C.1. Proof of Proposition 1

We prove the proposition in two steps, first by proving that the blur operator is equivariant to shifts, then that it is equivariant to rotations as long as the kernel is isotropic.

Let $x \in \mathbb{R}^n$ and $g_1, g_2 = 0, \dots, n' - 1$. Using (12) and Lemma 1, we compute

$$BT_{q_1,q_2}x = k * (T_{q_1,q_2}x)$$
 (23)

$$=T_{q_1,q_2}(k*x) (24)$$

$$=T_{g_1,g_2}Bx. (25)$$

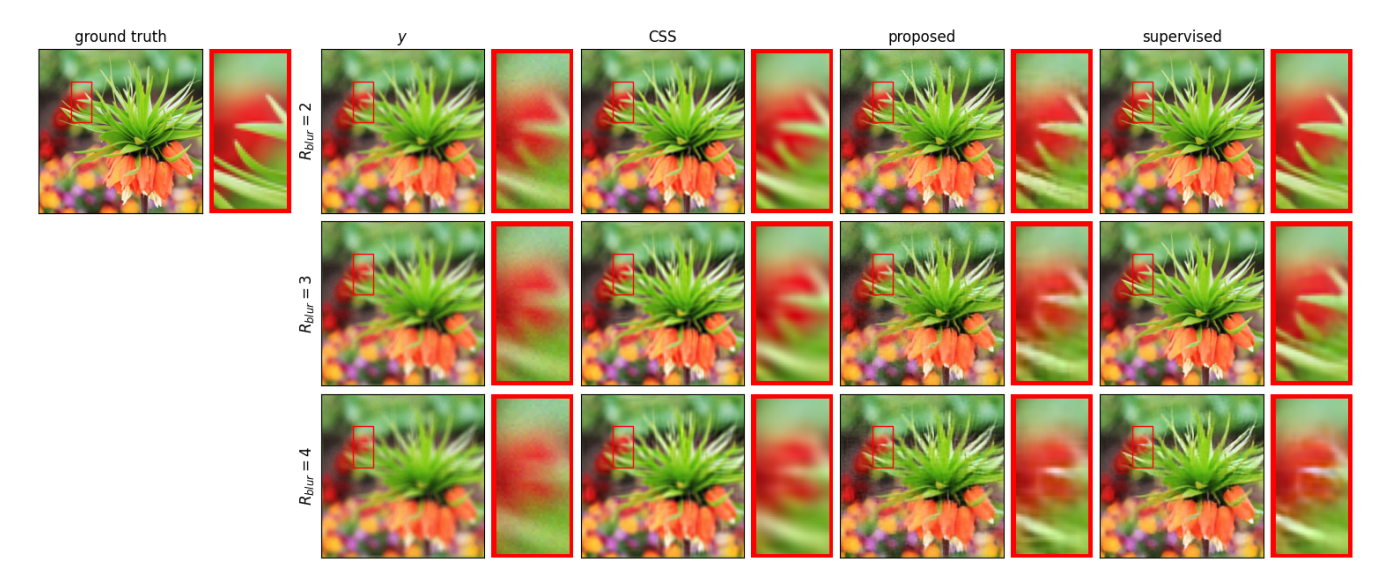


Figure 8. Sample reconstructions for Box deblurring on the validation split, for methods sup, proposed, and css, and different blur radii R_{blur} .

Thus the blur operator is equivariant to shifts.

Now, we assume that k is an isotropic kernel, and let g=0,90,180,270. Using (12) and Lemma 2 we compute

$$BR_{q}x = (k * (R_{q}x)), \tag{26}$$

$$=R_g(R_{g'}k*x), (27)$$

where $g' = (360 - g)_{n'}$. Then using (21) and (12) we compute

$$BR_q x = R_q(k * x) \tag{28}$$

$$= R_a B x. (29)$$

Thus the blur operator is equivariant to shifts.

Lemma 1. For $x, k \in \mathbb{R}^n$, and $g_1, g_2 = 0, ..., n' - 1$

$$k * (T_{q_1,q_2}x) = T_{q_1,q_2}(k * x).$$
 (30)

Proof. Let l, s = 0, ..., n' - 1,

$$[k * (T_{g_1,g_2}x)]_{l,s} = \sum_{p=0}^{n'-1} \sum_{q=0}^{n'-1} k_{p,q} [T_{g_1,g_2}x]_{(l-p)_{n'},(s-q)_{n'}}$$
(31)

$$= \sum_{p=0}^{n'-1} \sum_{q=0}^{n'-1} k_{p,q} x_{(l+g_1-p)_{n'},(s+g_2-q)_{n'}}$$

 $= (k * x)_{l+q_1, s+q_2} \tag{33}$

$$= [T_{g_1,g_2}(k*x)]_{l.s.} (34)$$

Lemma 2. For $k, x \in \mathbb{R}^n$, and g = 0, 90, 180, 270,

$$k * (R_q x) = R_q (R_{q'} k * x),$$
 (35)

where $g' = (360 - g)_{360}$.

Proof. We prove the four cases separately. First, if g = 0, then g' = 0, $R_g = R_{g'} = I_n$, and (35) is satisfied. If g = 90, then g' = 270, and using (11) and (15) we compute

$$(R_q((R_{q'}k)*x))_{l,s} = ((R_{q'}k)*x)_{(-s)_{n'},(l)_{n'}}$$
(36)

$$= \sum_{p=0}^{n'-1} \sum_{q=0}^{n'-1} (R_{g'}k)_{p,q} x_{(-s-p)_{n'},(l-q)_{n'}}$$
(37)

$$= \sum_{n=0}^{n'-1} \sum_{q=0}^{n'-1} k_{(q)_{n'},(-p)_{n'}} x_{(-s-p)_{n'},(l-q)_{n'}}$$
(38)

$$= \sum_{n=0}^{n'-1} \sum_{q=0}^{n'-1} k_{(q)_{n'},(p)_{n'}} x_{(-s+p)_{n'},(l-q)_{n'}}$$
(39)

$$=\sum_{p=0}^{n'-1}\sum_{q=0}^{n'-1}k_{p,q}x_{(-s+q)_{n'},(l-p)_{n'}}$$
(40)

$$= \sum_{p=0}^{n'-1} \sum_{q=0}^{n'-1} k_{p,q} (R_g x)_{(l-p)_{n'},(s-q)_{n'}}$$
(41)

$$= (k * (R_a x))_{l,s}. (42)$$

The cases g = 180 and g = 270 are proven similarly. \square

C.2. Proof of Proposition 2

We start by proving that the downsampling operator with anti-aliasing filter is equivariant to shifts, then we prove it is equivariant to rotations.

(32)

Let $x \in \mathbb{R}^n$, $g_1, g_2 = 0, \dots, n' - 1$, and $l, s = -(m' - 1)/2, \dots, (m'-1)/2$. Using (22), (14) and (16) we compute

$$(\hat{S}\hat{T}_{g_1,g_2}\hat{x})_{(l)_{m'},(s)_{m'}} = (\hat{T}_{g_1,g_2}\hat{x})_{(l)_{n'},(s)_{n'}}$$
(43)

$$= e^{2i\pi(lg_1 + sg_2)/n'} \hat{x}_{(l)_{n'},(s)_{n'}}$$
(44)

$$=e^{2i\pi(lg_1/2+sg_2/2)/m'}(\hat{S}\hat{x})_{l,s} \tag{45}$$

$$=(\hat{T}_{q_1,q_2}\hat{S}\hat{x})_{l,s}. (46)$$

Thus, the operator is equivariant to shifts.

Let g=0,90,180,270, and $l,s=-(m'-1)/2,\ldots,(m'-1)/2$. Using (22), Lemma 3 and Lemma 4, we compute

$$(\hat{S}\hat{R}_g\hat{x})_{(l)_{m'},(s)_{m'}} = (\hat{R}_g\hat{x})_{(l)_{n'},(s)_{n'}}$$
(47)

$$= (R_g \hat{x})_{(l)_{\pi'},(s)_{\pi'}} \tag{48}$$

$$= (\tilde{R}_g \hat{S} \hat{x})_{(l)_{m'},(s)_{m'}} \tag{49}$$

$$= (\tilde{R}_g \hat{S} \hat{x})_{(l)_{n'},(s)_{n'}}$$
 (50)

$$= (\hat{R}_g \hat{S} \hat{x})_{(l)_{n'},(s)_{n'}}. \tag{51}$$

Thus, the operator is equivariant to rotations.

Lemma 3. For g = 0, 90, 180, 270

$$\hat{R}_q = R_q. (52)$$

where $\hat{R}_q = \mathcal{F} R_a \mathcal{F}^{-1}$.

Proof. If g = 0, then $R_g = I_n$ and (52) is satisfied. If g = 90, let $x \in \mathbb{R}^n$, and $l, s = 0, \dots, n' - 1$. We compute

$$(\hat{R}_q \hat{x})_{l,s} = (\mathcal{F} R_q x)_{l,s} \tag{53}$$

$$= \sum_{n=0}^{n'-1} \sum_{g=0}^{n'-1} (R_g x)_{p,q} e^{-2i\pi(lp+sq)/n'}$$
 (54)

$$= \sum_{n=0}^{n'-1} \sum_{q=0}^{n'-1} x_{(-q)_n,(p)_n} e^{-2i\pi(lp+sq)/n'}$$
 (55)

$$=\sum_{n=0}^{n'-1}\sum_{q=0}^{n'-1}x_{p,q}e^{-2i\pi(-sp+lq)/n'}$$
(56)

$$= (\hat{x})_{(-s)_{n'},(l)_{n'}} \tag{57}$$

$$= (R_q \hat{x})_{l,s} \tag{58}$$

thus $\hat{R}_g=R_g$. If g=180 or g=270, we prove $\hat{R}_g=R_g$ similarly as in the g=90 case. \Box

Lemma 4. For g = 0, 90, 180, 270, $x \in \mathbb{R}^n$, and $l, s = -(m'-1)/2, \ldots, (m'-1)/2$,

$$(R_g \hat{x})_{(l)_{n'},(s)_{n'}} = (\tilde{R}_g \hat{S} \hat{x})_{(l)_{m'},(s)_{m'}}.$$
 (59)

Proof. For g=0, $R_g=I_n$ and $\tilde{R}_g=I_m$, then using (22) we obtain (59). If g=90, we compute

$$(R_g \hat{x})_{(l)_{n'},(s)_{n'}} = (\hat{x})_{(-s)_{n'},(l)_{n'}}$$
(60)

$$= (\hat{S}\hat{x})_{(-s)_{m'},(l)_{m'}} \tag{61}$$

$$= (\tilde{R}_g \hat{S} \hat{x})_{(l)_{m'},(s)_{m'}}. \tag{62}$$

The cases g=180 and g=270 can be proven similarly. \Box

D. Proof of Theorem 1

In this section, we prove that blurring and downsampling with an ideal anti-aliasing filter is not equivariant to down-scaling. Since an ideal anti-aliasing filter is a special case of blurring operator, it suffices to prove that blurring is not equivariant to downscaling, i.e. that for a signal $x \in \mathbb{R}^n$, and a scaling factor $g \in \{1/2, 1/3, \ldots\}$,

$$AT_q x \neq T_q A x.$$
 (63)

Without loss of generality, we prove the theorem for 1D signals. Extending the results to 2D signals is straightforward. We also assume that n is odd.

Blur transfer function The Fourier transform of a blur filter is typically nonzero around the zero-frequency, and in particular as long as the number of samples n is large enough,

$$\hat{a}_1 \neq 0. \tag{64}$$

Moreover, if the blur operator is not invertible, its Fourier transform \hat{a} vanishes for some frequency 0 < 1/q < n/2,

$$\hat{a}_{1/g} = 0.$$
 (65)

Symmetry of real filters Throughout the proof, we use the symmetry property of real filters (note that we work with real forward operators *A*), which satisfy

$$\hat{a}_l = \overline{\hat{a}}_{(n-l)_n}, \ l = 0, \dots, n-1$$
 (66)

where \overline{z} denote the complex conjugate of $z \in \mathbb{C}$.

Action by downscalings Downscaling in space consists of upscaling in frequency, in particular, a downscaling T_g by a factor $g \in \{1/2, 1/3, \ldots\}$ satisfies that

$$\hat{T}_g(\alpha \delta^{(1)} + \beta \delta^{(n-1)}) = \alpha \delta^{(1/g)} + \beta \delta^{(n-1/g)}$$
 (67)

where $\alpha, \beta \in \mathbb{C}$, and $\delta^{(l)}$ is a Dirac vector positioned at l, i.e. $\delta_s^{(l)} = 1$ if l = s, and $\delta_s^{(l)} = 0$ otherwise.

D.1. Proof

Consider a sinusoidal signal $x \in \mathbb{R}^n$ with Fourier transform

$$\hat{x} = \delta^{(1)} + \delta^{(n-1)}. (68)$$

We begin by showing that

$$AT_q x = 0. (69)$$

Letting $y^{(1)} := AT_g x$ and using (65), we have that

$$\begin{split} \hat{y}^{(1)} &= \hat{a} \cdot \hat{T}_g \hat{x}^{(1)} \\ &= \hat{a} \cdot \hat{T}_g (\delta^{(1)} + \delta^{(n-1)}) \\ &= \hat{a} \cdot (\delta^{(1/g)} + \delta^{(n-1/g)}) \\ &= \hat{a}_{1/g} \cdot \delta^{(1/g)} + \hat{a}_{n-1/g} \delta^{(n-1/g)} \\ &= \hat{a}_{1/g} \cdot \delta^{(1/g)} + \overline{\hat{a}}_{1/g} \delta^{(n-1/g)} \\ &= 0. \end{split}$$

Next we show that

$$T_q A x \neq 0. (70)$$

Letting $y^{(2)} := T_g Ax$ and using (64), we obtain

$$\begin{split} \hat{y}^{(2)} &= \hat{T}_g(\hat{a} \cdot \hat{x}) \\ &= \hat{T}_g(\hat{a} \cdot (\delta^{(1)} + \delta^{(n-1)})) \\ &= \hat{T}_g(\hat{a}_1 \cdot \delta^{(1)} + \hat{a}_{n-1}\delta^{(n-1)}) \\ &= \hat{a}_1 \cdot \delta^{(1/g)} + \hat{a}_{n-1}\delta^{(n-1/g)} \\ &= \hat{a}_1\delta^{(1/g)} + \overline{\hat{a}}_1\delta^{(n-1/g)} \\ &\neq 0. \end{split}$$

In summary, since we have that

$$AT_q x = 0 \neq T_q A x, (71)$$

i.e. the operator is not equivariant to downscalings.